How to cite: *Angew. Chem. Int. Ed.* **2023**, *62*, e202307436
doi.org/10.1002/anie.202307436

Water Sorption | Hot Paper

Consecutive Single-Crystal-to-Single-Crystal Isomerization of Novel Octamolybdate Anions within a Microporous Hybrid Framework with Robust Water Sorption Properties

Estibaliz Ruiz-Bilbao, Amaia Iturrospe, Santiago Reinoso, Beñat Artetxe, Garikoitz Beobide, Leire San Felices, Luis Lezama, Juan M. Gutiérrez-Zorrilla, Shaza Darwish, Debobroto Sensharma, and Michael J. Zaworotko*

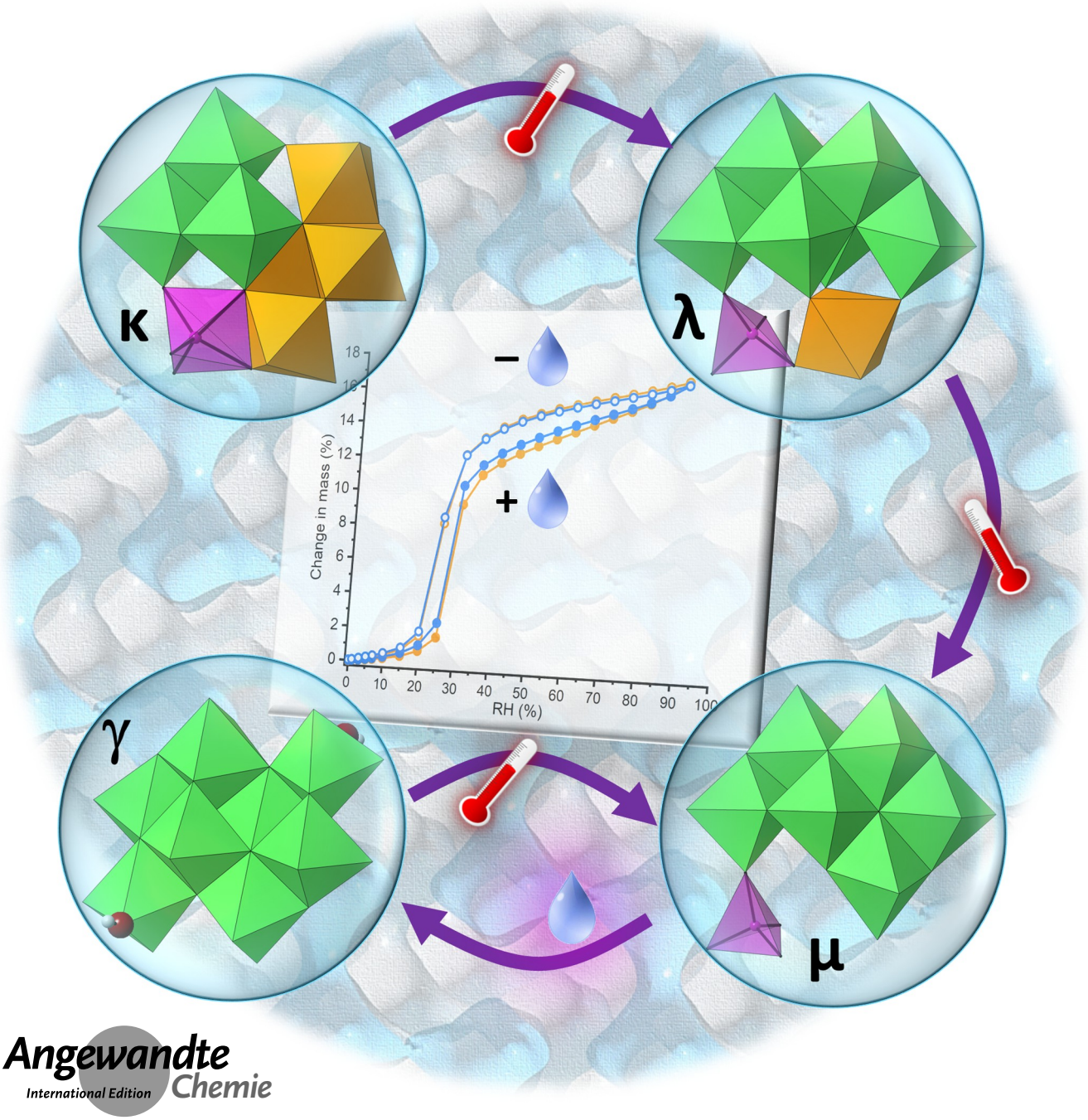

Abstract: The 3D hybrid framework $[\{Cu(cyclam)\}_3(\kappa\text{-}Mo_8O_{27})]\cdot 14H_2O$ (**1**) (cyclam = 1,4,8,11-tetraazacyclotetradecane) undergoes sequential single-crystal-to-single-crystal transformations upon heating to afford two different anhydrous phases (**2a** and **3a**). These transitions modify the framework dimensionality and enable the isomerization of κ-octamolybdate (κ-Mo_8) anions into λ (**2a**) and μ (**3a**) forms through metal migration. Hydration of **3a** involves condensation of one water molecule to the cluster to afford the γ-Mo_8 isomer in **4**, which dehydrates back into **3a** through the **6a** intermediate. In contrast, **2a** reversibly hydrates to form **5**, exhibiting the same Mo_8 cluster as that of **1**. It is remarkable that three of the Mo_8 clusters (κ, λ and μ) are new and that up to three different microporous phases can be isolated from **1** (**2a**, **3a**, and **6a**). Water vapor sorption analyses show high recyclability and the highest uptake values for POM-based systems. The isotherms display an abrupt step at low humidity level desirable for humidity control devices or water harvesting in drylands.

Introduction

The development of porous materials with capacity to adsorb gases and vapors represents a potential solution to current global challenges such as atmospheric pollution[1] and scarcity of freshwater.[2] Indeed, atmospheric water harvesting not only has the potential to address the global water shortage crisis, but also provides opportunities to fabricate practical devices for water purification,[3] dehumidification,[4] or indoor humidity control.[5] In this sense, Metal-Organic Frameworks (MOFs) are highly promising materials for gas sorption and separation,[6–7] because their modular constitution allows the fine-tuning of pore size and chemistry. However, water sorption could be challenging due to the limited hydrolytic stability displayed by some MOF families.[8–9] Incorporation of rigid, inorganic building-blocks that expose electronegative atoms toward the framework pores might improve the stability and selectivity toward polar adsorbates like water.[10]

In the past few years, polyoxometalate (POM)-based porous crystalline solids[11–12] have attracted great attention due to the possibility of combining the intrinsic multifunctionality of these clusters (e.g. catalysis, magnetism, or luminescence)[13] with the properties of extended open-framework architectures. Insoluble ionic crystals in which discrete metal-organic macrocations are combined with Keggin-type heteroPOMs $[XW_{12}O_{40}]^{n-}$ ($X{=}Co^{II}$, B^{III}, Si^{IV}, P^{V})[14] have exhibited selective water sorption properties,[15–16] because the non-efficient packing of such macro-ionic entities renders meaningful porosity to the structure. Another strategy involves the assembly of POMs with transition metal complexes acting as linkers. Some of us recently studied the use of Cu^{II} complexes of macrocyclic polyamines in which equatorial positions on the metal center are blocked by the multidentate ligand, leaving axial positions available for linking contiguous POM units. This approach led to different multifunctional materials, including the robust supramolecular framework $[Cu(cyclam)][\{Cu(cyclam)\}_2(V_{10}O_{28})]\cdot 10H_2O$ (cyclam = 1,4,8,11-tetraazacyclotetradecane), which selectively adsorbs CO_2 over N_2 and catalyzes the heterogeneous oxidation of adamantane,[17] as well as the $[\{Cu(cyclam)\}_3(W_7O_{24})]\cdot 15.5H_2O$ covalent hybrid with gas sorption capacity and the ability to undergo thermally-triggered single-crystal-to-single-crystal (SCSC) transformations.[18]

SCSC transformations allow for monitoring and gaining insight into how the location of atoms and molecules varies during a solid-state phase transition. The structural changes induced by external stimuli may modify key properties of the parent structure (e.g. magnetic, optical, or adsorptive) and lead to applications in sensing, selective storage, and molecular switches, among others. Furthermore, SCSC transformations can afford compounds showing peculiar architectures different from those obtained by conventional synthetic routes.

Although this property is difficult to achieve without the material losing crystallinity, tens of examples of SCSC transformations have been reported to date for coordination networks.[19] In comparison, examples are scarce for POM-based systems,[20] despite the fact that the largest change in a cell volume (ca. 2170 $Å^3$) observed for such kind of transformation corresponds to a solvent-mediated transition of the $Li_9K_7WCo_{10}[H_2P_8W_{48}O_{186}]$ salt.[21] The relative arrangement of POM units or counterions is usually modified during these

[*] E. Ruiz-Bilbao, Dr. B. Artetxe, Dr. G. Beobide, Prof. L. Lezama, Prof. J. M. Gutiérrez-Zorrilla
Departamento de Química Orgánica e Inorgánica, Facultad de Ciencia y Tecnología, Universidad del País Vasco UPV/EHU
P.O. Box 644, 48080 Bilbao (Spain)
E-mail: benat.artetxe@ehu.eus

Dr. A. Iturrospe
Centro de Física de Materiales (CSIC, UPV/EHU)
Paseo Manuel Lardizabal 5, 20018 Donostia-San Sebastián (Spain)

Dr. S. Reinoso
Departamento de Ciencias & Institute for Advanced Materials and Mathematics (InaMat2), Universidad Pública de Navarra (UPNA)
Campus de Arrosadia, 31006 Pamplona (Spain)

Dr. G. Beobide, Prof. J. M. Gutiérrez-Zorrilla
BCMaterials
Edificio Martina Casiano, 3rd Floor, UPV/EHU Science Park, Barrio Sarriena s/n, 48940 Leioa (Spain)

Dr. L. San Felices
Servicios Generales de Investigación SGIker, Facultad de Ciencia y Tecnología, Universidad del País Vasco UPV/EHU
P.O. Box 644, 48080 Bilbao (Spain)

Dr. S. Darwish, Dr. D. Sensharma, Prof. M. J. Zaworotko
Bernal Institute, Department of Chemical Sciences, University of Limerick
Limerick V94 T9PX (Ireland)

solid state reactions,[22] but no major skeletal modification of the metal-oxo cluster has been observed to date with the exception of i) an alkylammonium salt of $[\gamma\text{-}SiV_2W_{10}O_{39}]^{4-}$, which transforms its linear (μ-oxo)-divanadium(V) core into a bis(μ-hydroxo)-divanadium moiety when exposed to moisture;[23] and ii) the isomerization of $[B\text{-}H_2As_2Mo_6O_{26}(H_2O)]^{4-}$ to $[A\text{-}H_2As_2Mo_6O_{26}]^{4-}$ within a POM/metal–organic framework.[24]

The latter example belongs to our systematic studies on the $\{Cu(cyclam)\}^{2+}$/POM family, which has proven suitable for preparing hybrid coordination networks able to undergo SCSC transformations.[25] As part of our continuing investigations on the interaction between $\{Cu(cyclam)\}^{2+}$ and isopolymolybdates,[26] here we report the hybrid coordination network $[\{Cu(cyclam)\}_3(\kappa\text{-}Mo_8O_{27})]\cdot 14H_2O$ (**1**), which contains a novel octamolybdate (Mo_8) cluster (labeled κ) and undergoes sequential, thermally-induced SCSC transformations to afford two different anhydrous phases (**2a** and **3a**). Beyond relevant rearrangement of the Cu–O bonding scheme, these transitions involve isomerization of κ-Mo_8 into λ (**2a**) and μ (**3a**) forms through migration of Mo centers with variation of their coordination numbers. The three Mo_8 clusters are novel, thereby enlarging the catalog of as many as 9 different isomers reported to date.[27–29] The reversibility of these phase transitions has been studied and water vapor sorption properties analyzed for the microporous phases **2a** and **3a**.

Results and Discussion

Compound **1** was first obtained as a purple crystalline powder in ca. 15% yield from the reaction of commercial $(NH_4)_6[Mo_7O_{24}]$ and the *in situ* prepared $\{Cu(cyclam)\}^{2+}$ complex (1:3 stoichiometric ratio) in water at pH = 6.5, followed by addition of 1,4-dioxane. Samples suitable for single-crystal X-ray diffraction (SCXRD) were alternatively obtained by using hydrothermal methods. The infrared spectrum and powder X-ray diffraction (PXRD) pattern of the resulting prismatic crystals both fit well with those obtained for the polycrystalline samples (Figures S1–S3). For a more detailed Experimental Section, see the Supporting Information.

Motivated by the wide thermal stability range (ca. 100–230 °C) found in the thermogravimetric (TGA) curve of **1** upon dehydration (Figures S4–S5), variable temperature (VT) PXRD patterns were recorded from room temperature (RT) to 600 °C every 20 °C (Figure S6) to explore its thermostructural behavior, i.e. whether **1** shows crystallinity retention over amorphization with increasing temperature, and in the former case, whether it displays framework dynamism *vs* robustness. Results revealed that the hybrid coordination network retains crystallinity throughout the whole dehydration process and beyond up to 230 °C, in line with the thermal stability range found in the TGA curve. Upon heating, **1** rapidly transforms into a new crystalline phase (**2a**) as indicated by major modifications in both positions and relative intensities of the main diffraction peaks. In particular, the two intense maxima at $2\theta = 7.1°$ and 7.4° positions in **1** split into three different signals located at 7.3, 7.5, and 7.7° in **2a** (Figure S7). Moreover, the peak at 10.5° vanishes and new signals appear at 11.3, 22.5, and 23.2°. Considering that this transformation takes place at values close to RT, additional PXRD patterns were collected from 30 to 46 °C every 2 °C to explore this phase transition in depth (Figure S8). These experiments revealed that **2a** is already fully formed at 36 °C, and according to the TGA results, should correspond to a partially dehydrated phase. However, no mass loss associated with the release of H_2O molecules was observed in the TGA analyses carried out for a sample of **1** previously kept at 40 °C for 1 h to ensure its full conversion into **2a**. These observations suggest slow kinetics governing the removal of guest solvent molecules from **1**, and confirm the anhydrous nature of **2a**. Phase **2a** remains stable until 110 °C, but undergoes an additional transition above this temperature, transforming into a high-temperature anhydrous phase (**3a**), as indicated by the emergence of a new pair of most intense maxima at 7.4 and 7.8° with approx. 3:1 intensity ratio.

SCXRD data (Table S1) show that **1** crystallizes in the monoclinic space group $P2_1/n$ with an asymmetric unit (ASU) containing one $[\kappa\text{-}Mo_8O_{27}]^{6-}$ anion (**κ-Mo_8**), a total of three $\{Cu(cyclam)\}^{2+}$ complexes, of which two (Cu1A, Cu1B) are located in general positions and another two on centers of symmetry (Cu1C, Cu2C), and 14 H_2O molecules disordered over 20 sites (Figure S9). The **κ-Mo_8** anion is novel, thereby enlarging the current catalog of Mo_8 clusters in the literature (Table S2). It can be best described as one $\{Mo_4O_{16}\}$ tetramer and one $\{Mo_3O_{13}\}$ trimer fused by sharing one face and one corner between MoO_6 octahedra, with the eighth Mo center exhibiting square pyramidal geometry. The latter is connected to the tetramer by edge-sharing and to the trimer by sharing two corners (Figure 1a). To our knowledge, the Mo_8 species reported to date comprise up to nine different structural isomers for the $[Mo_8O_{26}]^{4-}$ anion, namely α, β, γ, δ, ε, ζ, η, θ and ι,[27–29] and a single isomeric form (γ) for the $\{Mo_8O_{28}\}^{6-}$ counterpart. The latter is a building block that can be found stabilized either by protonation in the $[Mo_8O_{26}(OH)_2]^{6-}$ anion,[30] or by polymerization,[26] resulting in $\{Mo_8O_{27}\}_n$ and $\{Mo_8O_{26}\}_n$ chain-like assemblies depending on the number of corners shared to polymerize. Despite the variety of MoO_x units ($x = 4$–6) and polyhedral connectivity shown in Table S2 for Mo_8 isomers, the face-sharing feature of **κ-Mo_8** is structurally novel.

All Cu^{II} centers display octahedral CuN_4O_2 geometry with cyclam N atoms in equatorial positions and terminal O_{POM} atoms occupying both axial positions. Significant Jahn–Teller distortion is present in all complexes, with the longest Cu1A–O_{POM} bond length of 2.876(5) Å being close to semi-coordination (Table S3). The crystal packing (Figure S10) reveals a 3-dimensional porous coordination network, in which hybrid layers of **κ-Mo_8** clusters linked to four neighbors through four bridging complexes (Cu1A, Cu1B, Cu1C, Cu2C) can be identified in the $(1\bar{1}0)$ plane (Figure 1b). This pattern results in rhombus-like grids with two types of voids arranged alternately along the crystallographic *z* axis. These grids are further connected through coordination of two additional complexes ($Cu1A^{i}$, $Cu1B^{ii}$; symmetry codes in Figure S10) to afford an open-framework architecture in which multiple C–H···O_{POM} and N–H···O_{POM} contacts estab-

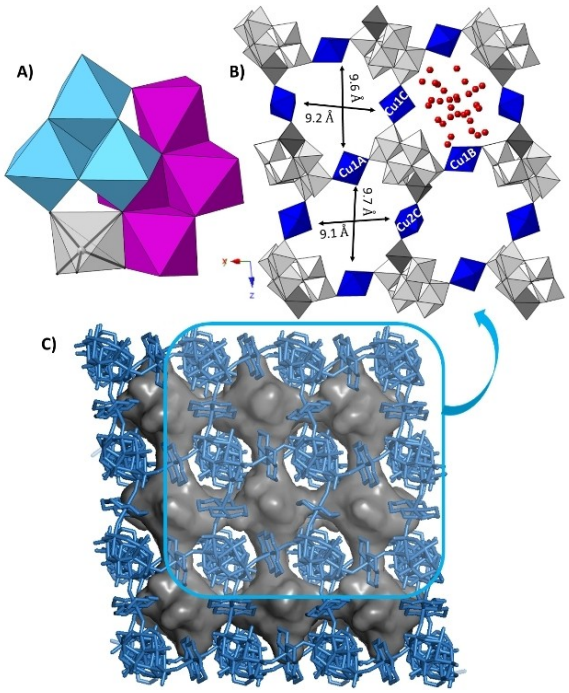

Figure 1. a) Polyhedral view of $[\kappa\text{-}Mo_8O_{27}]^{6-}$ (**κ-Mo$_8$**) ({Mo_4O_{16}} tetramer, pink; {Mo_3O_{13}}, light blue; {MoO_5}, gray). b) Projection of a hybrid layer of **1** on the (1$\bar{1}$0) plane ({MoO_5} polyhedra of **κ-Mo$_8$**, dark gray; {CuN_4O_2} octahedra, blue; O_w atoms, red spheres). c) Surface representation of interconnected water-filled channels in **1**.

lished between cyclam ligands and POM surfaces play a relevant reinforcing role (Table S4). The structure exhibits a 3-dimensional system of intersected, water-filled channels with cavities located at the space between 8 neighboring clusters and connected through narrow necks defined by 4 neighboring complexes (Figure 1c). The channels run along the [001], [1$\bar{1}$0] and [110] directions, their necks show cross-sections of ca. 9.7×9.1 and 9.6×9.2 Å (interatomic distances between opposite N atoms of the grid voids), and their total solvent accessible space accounts for 32 % of the unit cell volume.

To explore the structural changes that the thermally-triggered transitions above imply, SCXRD experiments were conducted on crystals of **1** heated for 1 h at 50 and 120 °C to ensure full transformation into the anhydrous **2a** and **3a** phases, respectively. For **2a**, dehydration results in a decrease of the unit cell volume to less than one-half of that of **1**, which is associated with the reduction of the cell symmetry to the triclinic $P\bar{1}$ space group. The ASU (Figure S11) now contains one $[\lambda\text{-}Mo_8O_{27}]^{6-}$ (**λ-Mo$_8$**) cluster and a total of three {Cu(cyclam)}$^{2+}$ moieties: one located in general positions (Cu1C) and four halves of centrosymmetric complexes (Cu1A, Cu2A, Cu1B, Cu2B).

The Mo_8 cluster undergoes κ to λ isomerization during the phase transition. This isomerization implies rupture of the face-sharing connection between {Mo_4O_{16}} and {Mo_3O_{13}} fragments observed in the κ form and formation of the edge-sharing {Mo_6O_{22}} moiety exhibited by the new λ-type anion, which is similar to the cap displayed by the well-known [β-Mo_8O_{26}]$^{8-}$ species (Figure 2a). This rearrangement proceeds via the rupture of two Mo-μ_3O bonds and the following consequent modifications: i) the seventh {MoO_6} octahedron goes from exclusively sharing edges in the κ form to exclusively sharing corners in the λ isomer, and ii) the eighth Mo center decreases its coordination number from five to four (tetrahedral geometry) and becomes linked to each of the fragments above by sharing one corner. Thus, solid-state migrations of some of the Mo centers take place within the cluster skeleton (Table S5 and Supporting Movies).

Regarding the crystal packing, hybrid layers in the (01$\bar{1}$) plane are analogous to those described for **1** but now the rhombus-like grid shows two void types of distinct size: those delimited by Cu1B and Cu1C, which are comparable in size to the voids in **1** (9.2×9.4 Å), and those defined by Cu2A and Cu1C with much smaller dimensions of 7.5×8.6 Å (Figure 2b). The connection between sheets is also different from that in **1** because only half of the {Cu(cyclam)}$^{2+}$ moieties located in the interlamellar space retain elongated octahedral geometry (Cu2B), whereas the other half becomes square planar (Figures S12–S13). The latter Cu1A complexes lose their character as covalent linkers, but still play a significant role in stabilizing the stacking of hybrid grids by establishing hydrogen bonding connectivity with tetrameric faces of **λ-Mo$_8$** clusters from adjacent sheets (Figure S12, Table S4). The connection between interlamellar cavities located at the space among clusters is disrupted through constrictions involving Cu1A and Cu2A fragments; hence, the 3-dimensional solvent-accessible network found in **1** is dismantled in **2a**.

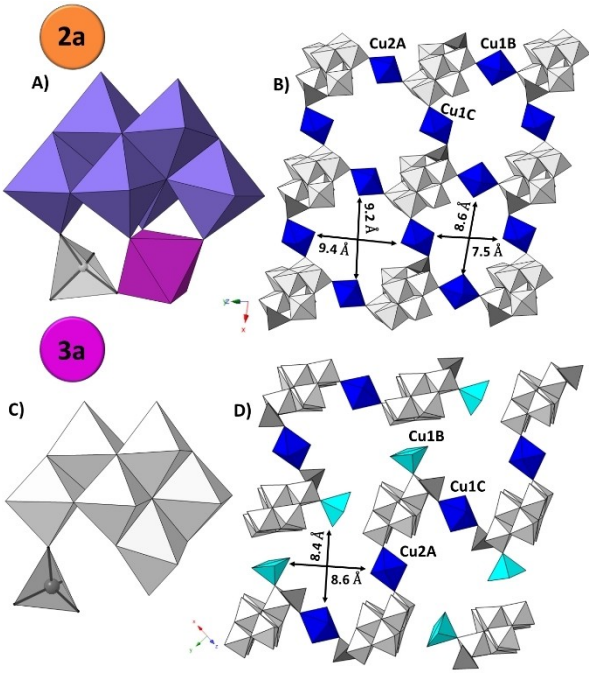

Figure 2. a) Polyhedral view of the **λ-Mo$_8$** isomer ({Mo_6O_{22}} hexamer, lilac; seventh {MoO_6}, pink; tetrahedral {MoO_4}, gray). b) Projection of a hybrid layer of **2a** on the (01$\bar{1}$) plane. c) Polyhedral view of the **μ-Mo$_8$** isomer ({Mo_7O_{24}} heptamer, light gray; tetrahedral {MoO_4}, dark gray). d) Projection of a supramolecular layer of **3a** on the (101) plane.

The resulting cavities nevertheless remain connected through strings of alternate wider and narrower windows arranged along the *y* axis in a zig-zag mode, giving rise to a porous system of parallel channels that diagonally intersect the stacking of hybrid layers (Figure S14). These pores are empty in **2a** and correspond to 24 % of the unit cell volume.

The second high-temperature anhydrous phase (**3a**) crystallizes in the same space group as **1** with the ASU (Figure S15) formed by one $[\mu\text{-}Mo_8O_{27}]^{6-}$ (**μ-Mo$_8$**) cluster, two $\{Cu(cyclam)\}^{2+}$ moieties in general positions (Cu1A, Cu1B), and another two halves of centrosymmetric complexes (Cu2A, Cu1C). The phase transition from **2a** to **3a** involves further isomerization of the Mo_8 cluster from the λ to the new μ form (Figure 2c). This process implies full edge-sharing condensation of the seventh $\{MoO_6\}$ unit in the λ isomer to the hexameric cap, resulting in a $\{Mo_7O_{24}\}$ fragment analogous to that displayed by $[\beta\text{-}Mo_8O_{26}]^{8-}$. As a result, the eighth Mo center becomes a tetrahedral $\{MoO_4\}$ antenna unit attached by a single corner-sharing linkage. It is noteworthy that the three Mo_8 isomers reported in this work are novel, evidencing that solid-state transformations can afford POMs that cannot be accessed by conventional solvent-mediated synthetic routes.

Compared to **1** and **2a**, the covalent 3-dimensional network is broken in **3a**, because the intralamellar moiety Cu1B loses its linking character and becomes a pentacoordinate appended unit with square-pyramidal geometry. Conversely, complexes Cu2A and Cu1C retain their bridging role in such a way that the **μ-Mo$_8$** anions are covalently linked into zig-zagging ribbons along the *y* axis (Figure 2d). The appended complexes nevertheless still play a key role in assembling such ribbons into supramolecular hybrid layers in the (101) plane through a massive hydrogen bonding network with the tetrameric faces of **μ-Mo$_8$** clusters (Figure S16, Table S4). The stacking of these supramolecular assemblies is facilitated by interlamellar Cu1A complexes, which in contrast to what observed for **2a**, are all octahedral covalent linkers (Figure S17). The porous network in **3a** consists also of a system of parallel channels, but in this case, the interlamellar cavities appear connected along the stacking [101] direction via the wide necks with ca. 8.6×8.4 Å cross-section that the formation of the pentacoordinate appended units opens. These empty pores account for 23 % of the unit cell volume.

To study the reversibility of the SCSC transitions above, samples of **2a** and **3a** were exposed to the laboratory atmosphere (LA: 15–20 °C; 40–50 % relative humidity, RH) and monitored by a combination of TGA and PXRD. With respect to **3a**, TGA analyses recorded after 1, 3, and 7 d of air exposure (Figures S18–S19) revealed that the anhydrous phase captures up to 12 H_2O molecules per POM after one week (% m, calcd 9.8; found 9.6), of which as many as 10 are adsorbed during the first 24 h. No additional H_2O molecules were adsorbed after 7 d of air exposure and the hydration/dehydration cycles in the resulting samples proved to be fully reversible. These results are in line with those from PXRD studies, which indicate that a new crystalline phase (**4**) different from the parent **1** starts forming when **3a** hydrates, but it is not fully formed until the seventh day of air exposure (Figure S20). In an attempt to promote a faster transformation, crystals of **3a** were placed in a more humid atmosphere and additional PXRD analyses demonstrated that formation of **4** could reach completion in just 24 h (Figure S21). In contrast, soaking the crystals in water for 1 h appeared to imply slight degradation, as evidenced by some additional poorly resolved maxima found in the experimental diffraction patterns (Figure S22). The reversibility of such transition was corroborated through VT-PXRD on **4** (Figure S23), which showed an intermediate phase (**6a**) in the transition from **4** to **3a** at 120 °C upon heating.

Considering the intricate crystal dynamics shown by this system, we tested whether the structure of **4** could be elucidated by SCXRD. Fortunately, the data acquired on a crystal of **3a** exposed to air for 7 days were suitable for a full structural resolution. Unluckily, we were not able to collect any data set of good quality for the intermediate **6a** despite testing several different crystal batches. Compound $[\{Cu(cyclam)\}_3\{\gamma\text{-}Mo_8O_{26}(OH)_2\}]\cdot 11H_2O$ (**4**) crystallizes in the triclinic $P\bar{1}$ space group and its ASU contains one-half of the well-known $\{\gamma\text{-}Mo_8O_{26}(OH)_2\}^{6-}$ species,[30] three halves of crystallographically independent $\{Cu(cyclam)\}^{2+}$ moieties and 5.5 H_2O molecules over 9 sites (Figure S24).

Formation of $[\gamma\text{-}Mo_8O_{26}(OH)_2]^{6-}$ in **4** (Figure 3a) implies that one H_2O molecule condenses to the POM skeleton and further dissociates along the hydration process. Protonation sites have been unequivocally assigned on the basis of Bond Valence Sum calculations (Table S6).[31] The isomerization of the Mo_8 anion to the more condensed, thermodynamically favored γ form after a full dehydration-phase transition-

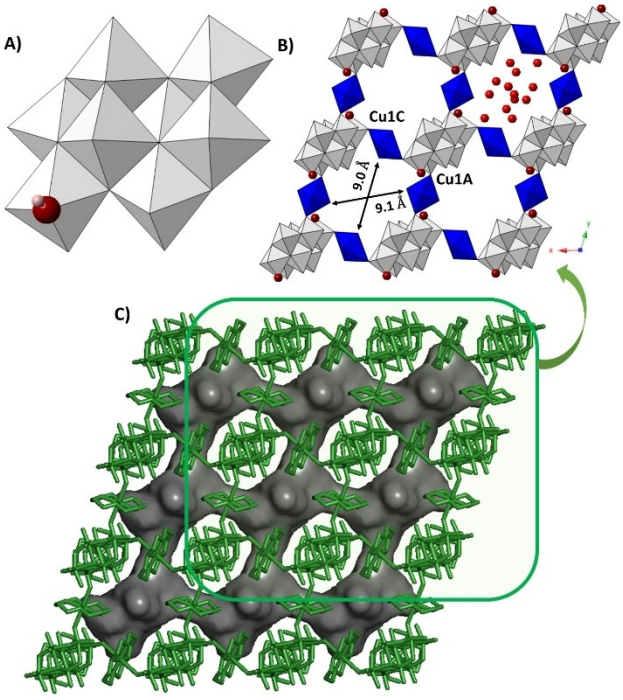

Figure 3. a) Polyhedral view of $[\gamma\text{-}Mo_8O_{26}(OH)_2]^{6-}$ (protonated O atoms, maroon spheres). b) Projection of a hybrid layer of **4** on the (001) plane. c) Surface representation of interconnected water-filled channels in **4**.

hydration cycle suggests that all the three previous isomers in **1**, **2a** and **3a** are obtained only because of the stabilization provided by the hydrogen bonding network established between cyclam ligands and surface O_{POM} atoms. Indeed, these weak but cooperative forces, together with the plasticity of Cu^{II} centers, might well be the key factor in allowing such a string of consecutive SCSC transformations in this system.[22]

The transformation of **3a** into **4** upon hydration implies that all $\{Cu(cyclam)\}^{2+}$ moieties regain their octahedral geometry and bridging role. Thus, each γ-Mo_8 unit is connected to six neighbors to give rise to a 3-dimensional covalent network reminiscent of that of **1** in which hybrid grids with square-like voids of cross-section 9.1×9.0 Å stack along the [001] direction (Figures 3b, S25). As in **1**, this architecture is pierced by a system of interconnected channels along the three crystallographic axes that host all the H_2O molecules (Figure 3c). The necks that communicate the wide cavities at the space between 8 neighboring clusters are somewhat narrower than those in **1**, hence the solvent-accessible space is slightly reduced to roughly 30 % of the unit cell volume.

In contrast to **3a**, hydration of **2a** upon air exposure was fully achieved in just 24 h (Figures S19, S26). Neither the number of adsorbed H_2O molecules calculated from TGA, nor the PXRD patterns of the resulting samples, matched any of the previous crystalline phases. This confirms the irreversibility of the transition from the parent hydrated phase **1** to the low-temperature anhydrous derivative **2a**. In fact, VT-PXRD patterns recorded every 2 °C for the cooling process of **2a** from 46 to 30 °C showed that a new phase (**5**) starts forming at RT within the experimental time-scale (Figure S27). The transition from **2a** to **5** is fully reversible as indicated by PXRD analyses carried out for **5** when heating from 30 to 100 °C every 5 °C (Figure S28).

The structure of the new hydrated phase **5** was determined on crystals of **2a** exposed to LA for 24 h to ensure full hydration. Compound $[\{Cu(cyclam)\}_3(\kappa\text{-}Mo_8O_{27})]\cdot 13H_2O$ (**5**) crystallizes in the triclinic $P\bar{1}$ space group with one **κ-Mo_8** anion, a total of three $\{Cu(cyclam)\}^{2+}$ complexes (Cu1B in general position; Cu1A, Cu2B, Cu1C, and Cu2C on centers of inversion), and 13 H_2O molecules over 16 sites in the ASU (Figure S29). It is noteworthy that **5** exhibits the same **κ-Mo_8** isomer as **1**, hence the κ to λ isomerization that takes place when going from **1** to **2a** is reversible despite such phase transition being irreversible. On the other hand, **5** displays the same space group as **2a** with very similar unit cell parameters, and therefore, this hydrated phase might be viewed as a transient state between parent **1** and anhydrous **2a**. In fact, preliminary experiments on the crystal dynamics triggered by vacuum in this system show that **5** generates upon dehydration of **1** in these conditions and subsequent partial hydration. Further studies on this matter will be reported in due course.

Regarding the crystal packing, the arrangement of POMs and bridging complexes within the hybrid layers in **5** is virtually identical to that in **2a** (Figure S30), but with the two distinct grid voids somewhat enlarged (9.1×8.7 and 9.6×9.4 Å) probably due to the breathing effect provided by the incorporation of H_2O molecules. In contrast to **2a**, no square-planar complexes are found in the interlamellar space as the stacking of hybrid layers along the $[01\bar{1}]$ direction is exclusively due to octahedral complex linkers. The resulting open framework displays a 2-dimensional interlamellar system of intertwined channels running along the [011] and [100] directions that host all H_2O molecules. These solvent-accessible regions are connected along the stacking direction only through the wider grid voids defined by Cu1B and Cu2C (Figure S31), accounting for 29 % of the unit cell volume. Figure 4 summarizes the intricate thermally-induced crystal dynamics shown by the title $\{Cu(cyclam)\}^{2+}/Mo_8$ system and the collection of SCSC transitions that relate the five crystal phases described in this work.[32]

Considering that **1** retains microporosity upon thermal removal of guest H_2O molecules, and that the pore windows are *a priori* wide enough to enable the diffusion of small molecule adsorbates, the gas sorption properties of the two different anhydrous phases in this work were evaluated. Figure 5 displays the results from N_2 (77 K) and CO_2 (195 K) sorption experiments carried out on crystalline samples of **1** activated at 50 and 120 °C under vacuum to ensure full conversion into **2a** and **3a**, respectively.

The N_2 adsorption curves correspond to type Ia isotherms typical of microporous materials with narrow pores (<1 nm). In both cases, micropores are filled rapidly at low relative pressures ($p/p^0<0.1$) to achieve saturation that extends up to $p/p^0=1$. The maximum gas uptake values for **2a** and **3a** (72 and 76 cm^3 (STP) g^{-1}, respectively) account for 6.4 and 6.8 adsorbed N_2 molecules per Mo_8 unit. The adsorption processes were observed to be completely reversible, and hence, all the gas molecules are desorbed at $p/p^0=0$. Fitting of both adsorption branches to the Brunauer–Emmett–Teller (BET) model[33] affords similar values of BET surface areas for **2a** and **3a** (302 and 298 $m^2 g^{-1}$). Although these values are much lower than the highest areas reported for POM-loaded MOFs (>1000 $m^2 g^{-1}$),[34–35] our results are comparable to those displayed by some other POM-metalorganic frameworks, such as $[Cu(cyclam)][\{Cu(cyclam)\}_2(V_{10}O_{28})]$ (205 $m^2 g^{-1}$),[16] or $(TBA)_2[Cu(BBTZ)_2(\alpha\text{-}Mo_8O_{26})]$

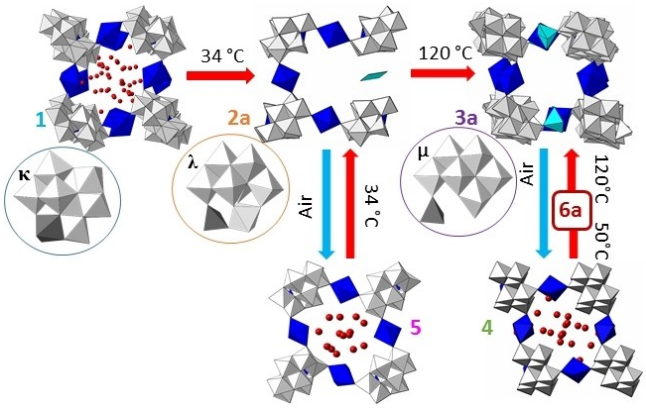

Figure 4. Scheme of the SCSC transformations reported in this work.

(773 $m^2 g^{-1}$; BBTZ = 1,4-bis(1,2,4-triazol-1-ylmethyl)-benzene).[36]

In regard to the CO_2 uptake isotherms, saturation is roughly achieved at much higher relative pressures ($p/p^0 = 1.0$). The adsorption processes were also observed to be fully reversible and the maximum uptakes were also found to reach very similar values for **2a** and **3a** (66 and 64 cm^3 (STP) g^{-1}), accounting for 5.9 and 5.7 adsorbed CO_2 molecules per Mo_8 unit. In contrast to what we observed in related POM/Cu(cyclam) porous frameworks, in which N_2 adsorption was negligible[16] or the maximum uptake accounted for only 30 % of the simulated value,[17] both N_2 and CO_2 are readily adsorbed by **2a** and **3a**. This fact encouraged us to carry out additional experiments at different temperatures to gain a better understanding of the adsorptive properties of such anhydrous phases and to test their performance in purification or selective capture of small molecule gas mixtures. These results will be reported elsewhere in due course.

The reversible nature of the transitions from **2a** to **5** and from **3a** to **4** motivated us to study the water-vapor sorption properties of our thermally-activated microporous materials. Dynamic vapor sorption (DVS) experiments were conducted at 298 K from vacuum to 90 % RH for both anhydrous phases. For **2a**, the adsorption isotherm indicates that pores remain virtually empty up to almost 20 % of RH. After this point, a sudden increase of the water uptake occurs with a steep step that reaches ca. 70 % of the total capacity at 35 % RH. The maximum uptake at 90 % RH represents an increase of 16.4 % of the total mass with respect to that of **2a** (Figure 6a). Small differences between the calculated mass for the 13 H_2O molecules in the resulting hydrated phase **5** and the values found experimentally (Table S7) could arise from the surface condensation that can take place in the intergranular space.[2] These values result in a maximum working capacity of 222 $cm^3 g^{-1}$ for **2a**, which is one of the highest values observed to date for POM-based water sorbents (see Table S8 for literature uptake values of related compounds and associated discussion, including a brief comparison to zeolites and MOFs). The desorption process is almost superimposable to the adsorption, which suggests full reversibility. In order to confirm its cyclability, a second isotherm was measured under the same conditions and the working capacity remained virtually identical (218 $cm^3 g^{-1}$, 16.2 % change in mass at 90 % RH). PXRD analyses on **2a** verified retention of crystallinity after the adsorption/desorption processes (Figure S32).

With respect to **3a**, this phase does not adsorb any significant amount of water below 15 % RH. From this point, a steep water uptake is observed up to 35 % RH, after which the slope of the adsorption profile decreases. This slower step extends up to 50 % RH and accounts for the mass of a single H_2O molecule. This observation could result from the structural transition from **3a** to **4** associated with the incorporation of one H_2O molecule to the POM skeleton and subsequent structural rearrangement from $[\mu\text{-}Mo_8O_{27}]^{6-}$ to $[\gamma\text{-}Mo_8O_{26}(OH)_2]^{6-}$ (Figure 6b). After reaching a maximum working capacity of 235 $cm^3 g^{-1}$ (17.4 % change in mass) at 90 % RH, the desorption process suggests that the $[\gamma\text{-}Mo_8O_{26}(OH)_2]^{6-}$ anion remains stable upon dehydration because one

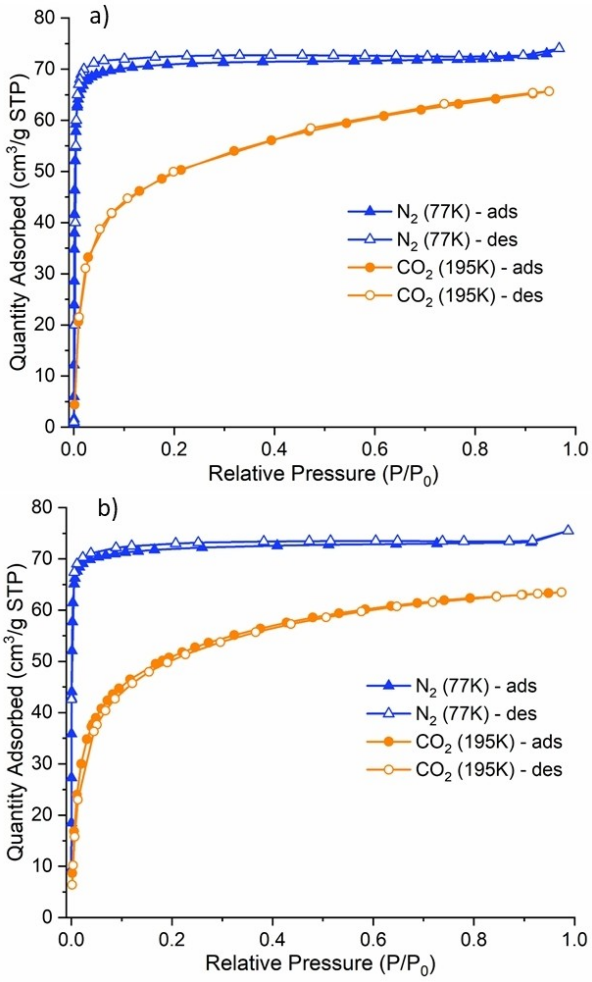

Figure 5. N_2 and CO_2 isotherms for a) **2a** and b) **3a**. Filled and empty markers correspond to adsorption and desorption branches, respectively.

H_2O molecule is retained in the active material. PXRD analyses (Figure S33) confirmed that **4** does not revert back to **3a** under vacuum and indicate that the third anhydrous phase (**6a**) could be generated as a result. The PXRD pattern of this phase fits well with that observed for a sample of **4** treated under vacuum (Figure S34), as well as, to that of the intermediate phase found in the thermal transition from **4** to **3a** upon heating (Figure S23). FTIR spectra suggest the presence of the γ-Mo_8 isomer in **6a**, albeit inconclusively (Figure S35). The distinct adsorption/desorption processes made us record additional cycles (Figure 6c). The reversibility of the water uptake between phases **4** and **6a** was confirmed because both curves were virtually identical and they showed a maximum working capacity of 223 $cm^3 g^{-1}$ at 90 % RH (16.5 % change in mass).

Besides the total capacity, the cyclability of the system and sorption kinetics are also important factors that should be taken into account for utility. Considering that i) the steep uptake takes place at 20–35 % RH range in all cases, and ii) 80 % of the total capacity is reached at 60 % RH (standard working conditions for some common commercial

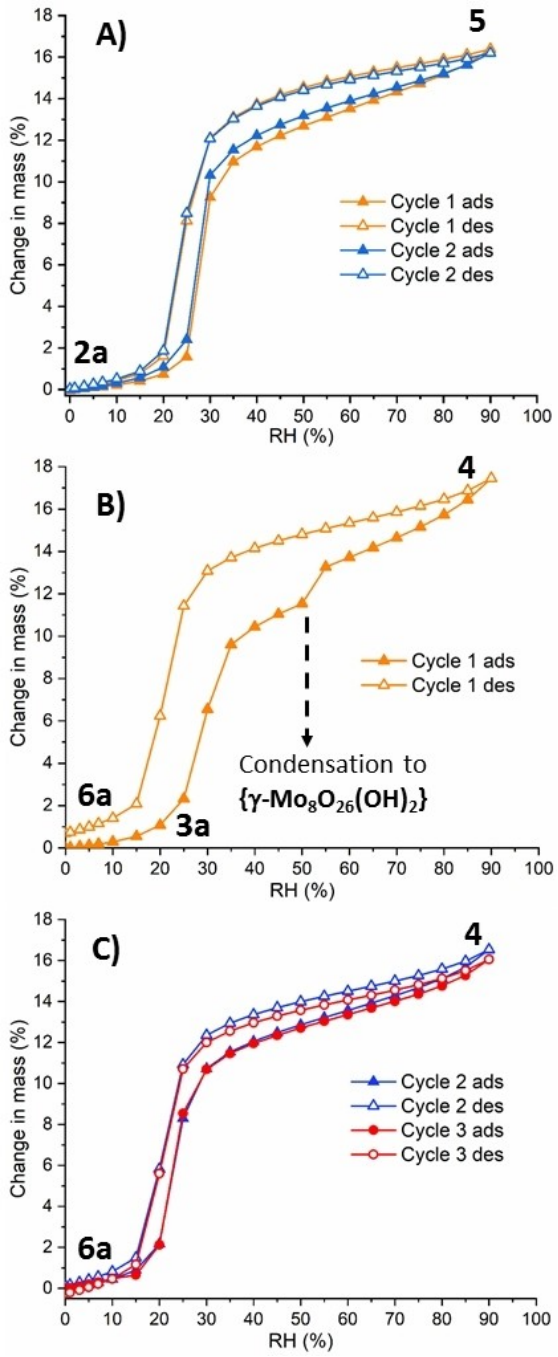

Figure 6. DVS isotherms from 0 to 90% relative humidity at 298 K for a) **2a** (2 cycles), and **3a**, b) first cycle leading to **6a**, c) second and third cycles.

desiccants),[37] the kinetics of these two processes were studied at a constant vapor flow rate of 30 and 60 % RH, respectively. Under low humidity vapor flow swing (0–30–0 % RH), water uptake took as long as 100 min to be completed (Figures S36–S37), whereas both adsorption and desorption processes are achieved in less than 15 min at a RH swing of 0–60–0 % for both phases at RT.

The durability and recyclability of the adsorbents were evaluated by 100 cycles of water adsorption-desorption experiments at 298 K and a constant vapor flow rate of 0–60–0 % RH. Plots in Figures S36 and S37 show an average water uptake of 14 % and 13 % for **2a** and **6a**, respectively, values that are very close to those observed in the initial isotherms. Thus, the regeneration of the materials occurs after 100 cycles under humidity swing conditions. Materials with this type of relatively fast, reversible behavior are suited for their use in heat pumps or air conditioners.[38] Moreover, the fast kinetics and reproducibility of the adsorption-desorption process make these materials potentially suitable for dehumidification in confined spaces, as well as, for water harvesting and purification in drylands.[39–41]

Conclusion

This work nicely exemplifies the potential of solid-state transitions to afford novel POM clusters that cannot be accessed by classical solvent-mediated synthesis. The extended framework $[\{Cu(cyclam)\}_3(\kappa\text{-}Mo_8O_{27})]\cdot 14H_2O$ (**1**) represents one of the rare examples of POM-based systems that can undergo up to four SCSC transformations related to thermal dehydration-hydration processes. Removal of H_2O molecules sequentially affords the anhydrous $[Cu(cyclam)][\{Cu(cyclam)\}_2(\lambda\text{-}Mo_8O_{27})]$ (**2a**) and $[\{Cu(cyclam)\}_3(\mu\text{-}Mo_8O_{27})]$ (**3a**) phases upon heating. These transitions imply two consecutive isomerizations of Mo_8 anions through solid-state metal migration from a κ form with unusual face-sharing connectivity between $\{MoO_6\}$ octahedra to a μ form reminiscent of the most usual β isomer but with an appended $\{MoO_4\}$ tetrahedral unit. It is noteworthy that the three κ-, λ-, and μ-Mo_8 isomers in this work have never been reported before. Hydration of **3a** upon air exposure involves condensation-dissociation of one H_2O molecule to the POM cluster to result in the known γ isomer that is found in $[\{Cu(cyclam)\}_3\{\gamma\text{-}Mo_8O_{26}(OH)_2\}]\cdot 11H_2O$ (**4**), which dehydrates into the third anhydrous phase **6a** before reverting back to **3a**. In contrast, **2a** hydrates to form $[\{Cu(cyclam)\}_3(\kappa\text{-}Mo_8O_{27})]\cdot 13H_2O$ (**5**), which displays the same Mo_8 cluster as **1**, proving the reversibility of the κ to λ isomerization. Water vapor sorption isotherms of the anhydrous phases display an abrupt step at low relative humidity level (20–30 %) that, together with a high cyclability (>100 cycles), could be desirable for humidity control devices in confined spaces, or water harvesting and purification systems in drylands. Their associated uptake values are among the highest reported to date for POM-based systems. The fact that **1** can afford three different microporous phases (**2a**, **3a**, and **6a**) could endow this system with the capacity to selectively adsorb different molecules depending on its activation procedure. Studies on the ability of these phases to undergo selective adsorption from mixtures of gases will be carried out in the near future.

Acknowledgements

Funded by Eusko Jaurlaritza/Gobierno Vasco (EJ/GV, grants IT1722-22 and KK-2022/00045). E.R.B. thanks EJ/GV for her doctoral fellowship (PRE_2018_1_0143). Tech-

nical and human support from SGIker (UPV/EHU) is gratefully acknowledged.

Conflict of Interest

The authors declare no conflict of interest.

Data Availability Statement

The data that support the findings of this study are available from the corresponding author upon reasonable request.

Keywords: Microporous Materials · Polyoxometalates · Single-Crystal-to-Single-Crystal · Solid-State Isomerization · Water Sorption

[1] Ed. S. K. Ghosh, *Metal-Organic Frameworks (MOFs) for Environmental Applications*, Elsevier, Amsterdam **2019**.
[2] J. Canivet, A. Fateeva, Y. Guo, B. Coasne, D. Farrusseng, *Chem. Soc. Rev.* **2014**, *43*, 5594–5617.
[3] Y. Song, J. Phipps, C. Zhu, S. Ma, *Angew. Chem. Int. Ed.* **2023**, *62*, e202216724.
[4] S. Cui, M. Qin, A. Marandi, V. Steggles, S. Wang, X. Feng, F. Nouar, C. Serre, *Sci. Rep.* **2018**, *8*, 15284.
[5] N.-X. Zhu, Z.-W. Wei, C.-X. Chen, X.-H. Xiong, Y.-Y. Xiong, Z. Zeng, W. Wang, J.-J. Jiang, Y.-N. Fan, C.-Y. Su, *Angew. Chem. Int. Ed.* **2022**, *61*, e202112097.
[6] T. He, X.-J. Kong, Z.-X. Bian, Y.-Z. Zhang, G.-R. Si, L.-H. Xie, X.-Q. Wu, H. Huang, Z. Chang, X.-H. Bu, M. J. Zaworotko, Z.-R. Nie, J.-R. Li, *Nat. Mater.* **2022**, *21*, 689–695.
[7] J.-R. Li, R. J. Kuppler, H.-C. Zhou, *Chem. Soc. Rev.* **2009**, *38*, 1477–1504.
[8] G. Férey, C. Mellot-Draznieks, C. Serre, F. Millange, J. Dutour, S. Surblé, I. Margiolaki, *Science* **2005**, *309*, 2040–2042.
[9] S. S.-Y. Chui, S. M.-F. Lo, J. P. H. Charmant, A. G. Orpen, I. D. Williams, *Science* **1999**, *283*, 1148–1150.
[10] H. S. Scott, M. Shivanna, A. Bajpai, D. G. Madden, K.-J. Chen, T. Pham, K. A. Forrest, A. Hogan, B. Space, J. J. Perry, M. J. Zaworotko, *ACS Appl. Mater. Interfaces* **2017**, *9*, 33395–33400.
[11] L. Vilà-Nadal, L. Cronin, *Nat. Rev. Mater.* **2017**, *2*, 17054.
[12] D.-Y. Du, J.-S. Qin, S.-L. Li, Z.-M. Su, Y.-Q. Lan, *Chem. Soc. Rev.* **2014**, *43*, 4615–4632.
[13] M. T. Pope, *Heteropoly and Isopoly Oxometalates*, Springer, Berlin **1983**.
[14] Y. Shimoyama, S. Uchida, *Chem. Lett.* **2021**, *50*, 21–30.
[15] S. Uchida, N. Mizuno, *J. Am. Chem. Soc.* **2004**, *126*, 1602–1603.
[16] S. Uchida, R. Eguchi, N. Mizuno, *Angew. Chem. Int. Ed.* **2010**, *49*, 9930–9934.
[17] J. Martín-Caballero, A. S. J. Wéry, S. Reinoso, B. Artetxe, L. San Felices, B. El Bakkali, G. Trautwein, J. Alcañiz-Monge, J. L. Vilas, J. M. Gutiérrez-Zorrilla, *Inorg. Chem.* **2016**, *55*, 4970–4979.
[18] J. Martín-Caballero, B. Artetxe, S. Reinoso, L. San Felices, O. Castillo, G. Beobide, J. L. Vilas, J. M. Gutiérrez-Zorrilla, *Chem. Eur. J.* **2017**, *23*, 14962–14974.
[19] E. Fernandez-Bartolome, A. Martinez-Martinez, E. Resines-Urien, L. Piñeiro-Lopez, J. Sanchez-Costa, *Coord. Chem. Rev.* **2022**, *452*, 214281.
[20] S. Reinoso, B. Artetxe, L. San Felices, J. M. Gutiérrez-Zorrilla, *Polyoxometalates. Properties, Structure and Synthesis* (Ed. A. P. Roberts), Nova Science, Hauppauge, NY **2016**, pp 143–212.
[21] C. Zhan, J. M. Cameron, D. Gabb, T. Boyd, R. S. Winter, L. Vilà-Nadal, S. G. Mitchell, S. Glatzel, J. Breternitz, D. H. Gregory, D.-L. Long, A. Macdonell, L. Cronin, *Nat. Commun.* **2017**, *8*, 14185.
[22] S. Reinoso, B. Artetxe, J. M. Gutiérrez-Zorrilla, *Acta Crystallogr. Sect. C* **2018**, *74*, 1222–1242.
[23] K. Uehara, N. Mizuno, *J. Am. Chem. Soc.* **2011**, *133*, 1622–1625.
[24] N. Dissem, B. Artetxe, L. San Felices, G. Beobide, O. Castillo, E. Ruiz-Bilbao, L. Lezama, M. dM Vivanco, A. Haddad, J. M. Gutiérrez-Zorrilla, *Inorg. Chem.* **2021**, *60*, 14913–14923.
[25] L. Fernández-Navarro, A. Iturrospe, S. Reinoso, B. Artetxe, E. Ruiz-Bilbao, L. San Felices, J. M. Gutiérrez-Zorrilla, *Cryst. Growth Des.* **2020**, *20*, 3499–3509.
[26] N. Dissem, B. Artetxe, L. San Felices, L. Lezama, A. Haddad, J. M. Gutiérrez-Zorrilla, *Crystals* **2018**, *8*, 20.
[27] A. J. Bridgeman, *J. Phys. Chem. A* **2002**, *106*, 12151–12160.
[28] D. G. Allis, E. Burkholder, J. Zubieta, *Polyhedron* **2004**, *23*, 1145–1152.
[29] Z.-C. Yue, H.-J. Du, Y.-Y. Niu, G.-X. Jin, *CrystEngComm* **2013**, *15*, 9844–9848.
[30] M. Isobe, F. Marumo, T. Yamase, T. Ikawa, *Acta Crystallogr. Sect. B* **1978**, *34*, 2728–2731.
[31] I. D. Brown, K. K. Wu, *Acta Crystallogr. Sect. B* **1976**, *32*, 1957–1959.
[32] Deposition numbers 2246884 (for **1**), 2246885 (for **2a**), 2246886 (for **3a**) 2246887 (for **4**) and 2246888 (for **5**) contain the supplementary crystallographic data for this paper. These data are provided free of charge by the joint Cambridge Crystallographic Data Centre and Fachinformationszentrum Karlsruhe Access Structures service.
[33] S. Brunauer, P. H. Emmett, E. Teller, *J. Am. Chem. Soc.* **1938**, *60*, 309–319.
[34] H. N. Miras, L. Vilà-Nadal, L. Cronin, *Chem. Soc. Rev.* **2014**, *43*, 5679–5699.
[35] C. T. Buru, P. Li, B. L. Mahdi, A. Dohnalkova, A. E. Platero-Prats, N. D. Browning, K. W. Chapman, J. T. Hupp, O. K. Farha, *Chem. Mater.* **2017**, *29*, 5174–5181.
[36] H. Fu, C. Qin, Y. Lu, Z.-M. Zhang, Y.-G. Li, Z.-M. Su, W.-L. Li, E.-B. Wang, *Angew. Chem. Int. Ed.* **2012**, *51*, 7985–7989.
[37] Y.-K. Seo, J. W. Yoon, J. S. Lee, Y. K. Hwang, C.-H. Jun, J.-S. Chang, S. Wuttke, P. Bazin, A. Vimont, M. Daturi, S. Bourrelly, P. L. Llewellyn, P. Horcajada, C. Serre, G. Férey, *Adv. Mater.* **2012**, *24*, 806–810.
[38] L. Chen, C. He, *Microporous Mesoporous Mater.* **2020**, *305*, 110378–110386.
[39] K. Zu, M. Qin, S. Cui, *Renewable Sustainable Energy Rev.* **2020**, *133*, 110246.
[40] H. Furukawa, F. Gándara, Y.-B. Zhang, J. Jiang, W. L. Queen, M. R. Hudson, O. M. Yaghi, *J. Am. Chem. Soc.* **2014**, *136*, 4369–4381.
[41] S. M. Towsif Abtab, D. Alezi, P. M. Bhatt, A. Shkurenko, Y. Belmabkhout, H. Aggarwal, Ł. J. Weseliński, N. Alsadun, U. Samin, M. N. Hedhili, M. Eddaoudi, *Chem* **2018**, *4*, 94–105.

Manuscript received: May 26, 2023
Accepted manuscript online: June 15, 2023
Version of record online: June 30, 2023